Supplementary Information for:

Structural mechanisms for the activation of human cardiac KCNQ1 channel by electro-mechanical coupling enhancers

Demin Ma[a,1], Ling Zhong[b,1], Zhenzhen Yan[b], Jing Yao[a], Yan Zhang[a], Fan Ye[a], Yuan Huang[c], Dongwu Lai[d], Wei Yang[a,e,f,2], Panpan Hou[b,2], Jiangtao Guo[a,d,e,f,g,h,2]

[a] Department of Biophysics, and Department of Neurology of the Fourth Affiliated Hospital, Zhejiang University School of Medicine, Hangzhou, Zhejiang 310058, China;

[b] Dr. Neher's Biophysics Laboratory for Innovative Drug Discovery, State Key Laboratory of Quality Research in Chinese Medicine, Macau University of Science and Technology, Taipa, Macao SAR, China

[c] Department of Cardiology, First Affiliated Hospital, Zhejiang University School of Medicine, Hangzhou, Zhejiang 310058, China;

[d] Department of Cardiology, Key Laboratory of Cardiovascular Intervention and Regenerative Medicine of Zhejiang Province, Sir Run Run Shaw Hospital, Zhejiang University School of Medicine, Hangzhou, Zhejiang 310016, China

[e] Liangzhu Laboratory, Zhejiang University Medical Center, 1369 West Wenyi Road, Hangzhou, Zhejiang 311121, China

[f] NHC and CAMS Key Laboratory of Medical Neurobiology, MOE Frontier Science Center for Brain Science and Brain-machine Integration, School of Brain Science and Brain Medicine, Zhejiang University

[g] State Key Laboratory of Plant Physiology and Biochemistry, College of Life Sciences, Zhejiang University, Hangzhou, Zhejiang 310058, China

[h] Cancer Center, Zhejiang University, Hangzhou, Zhejiang 310058, China

[1] These authors contributed equally to this work.

[2] Correspondence: jiangtaoguo@zju.edu.cn (J.G.), pphou@must.edu.mo (P.H.), yangwei@zju.edu.cn (W.Y.)

This PDF file includes:

Supplementary Materials and Methods

Supplementary Fig. S1-S10

Supplementary Table S1

Supplementary Movie Legends

Supplementary References

Supplementary Materials and Methods

Protein expression and purification

The full-length human KCNQ1 gene was synthesized and cloned into the modified pEZT-BM vector with a C-terminal strep tag. The human CaM gene was cloned into pEZT-BM vector with a C-terminal Histidine tag. KCNQ1 and CaM complex were heterologously expressed in Human Embryonic Kidney (HEK) 293S suspension cells (Life Technologies) maintained at 30 °C in SMM 293-TI complete medium (Sino Biological Inc.) supplemented with 2% fetal bovine serum (FBS, Yeasen Biotechnology (Shanghai) Co., Ltd.). The P3 baculovirus was generated via the BacMam system (Thermo Fisher Scientific) and used for expression when cell density reached 3.5×10^6 cells/mL. P3 baculovirus mixture of KCNQ1: CaM (6:1) was used for transduction of HEK293S cells for protein expression. To boost protein expression, 10 mM sodium butyrate was added 12 h post-transduction. Cells were harvested after 48 h, then flash-frozen in liquid nitrogen and stored at -80 °C until needed.

Cells were resuspended and lysed by sonication in buffer A (20 mM Tris, pH 8.0, 150 mM KCl, 3 mM DTT) supplemented with a protease inhibitor cocktail (2 µg/mL DNase I, 0.5 µg/mL pepstatin, 2 µg/mL leupeptin, 1 µg/mL aprotinin, and 1 mM PMSF). The lysate was then solubilized with 1.5% n-dodecyl-β-D-maltoside (DDM, Anatrace) and 0.3% cholesteryl hemisuccinate tris salt (CHS, Anatrace) at 4°C for 3 h. The insoluble cell fragment was removed by centrifugation at 48,000g for 50 min at 4°C. The supernatant was incubated with Strep-Tactin Sepharose resin (IBA) at 4°C for 1.5 h with gentle rotation. Beads were loaded onto a gravity column and washed with buffer B (buffer A supplemented with 0.05% DDM and 0.01% CHS) for 4 CVs (column volumes), followed by washing with buffer C (buffer A supplemented with 0.03% GDN) for 16 CVs. The protein was then eluted with buffer C plus 10 mM d-Desthiobiotin (Sigma) and further purified on a Superose 6 gel filtration column (GE Healthcare) in buffer D (buffer A supplemented with 4mM EGTA). The peak fraction was collected and concentrated for cryo-EM sample preparation. The typical yield of KCNQ1-CaM is about 3.4 mg from 1 L HEK293S cell culture. For KCNQ1-$\text{CaM}_{\text{ML277}}$ structure, the purified protein was incubated with 0.125 mM ML277 (MedChemExpress), for KCNQ1-$\text{CaM}_{\text{ML277-PIP2}}$ structure, the protein was incubated with 0.125 mM ML277 and 1 mM PIP_2. The PIP_2 we used is 1,2-dioctanoyl-sn-glycero-3-phospho-(1'-myo-inositol-4',5'-bisphosphate) (ammonium salt) purchased from Avanti.

Cryo-EM sample preparation and data acquisition

For grids preparation, 3 μL concentrated protein was loaded onto glow-discharged R1.2/1.3 Quantifoil grids at 4°C under 100% humidity. Grids were blotted for 4.5 seconds and plunge-frozen in liquid ethane using a Vitrobot Mark IV (FEI). Micrographs were acquired on a Titan Krios microscope (FEI) operated at a voltage of 300 kV with a K2 summit direct electron detector (Gatan) via SerialEM (1) following standard procedure. A calibrated magnification of 49310× was used for imaging, yielding a pixel size of 1.014 Å. The defocus range was set from -1.1 μm to -1.3 μm. Micrographs were dose-fractionated to 40 frames with a dose rate of 8 e^-/pixel/s and a total exposure time of 8 s, corresponding to a total dose of ~64 $e^-/Å^2$.

Image processing

Motion correction and CTF parameters estimation were performed with the MotionCorr2 (2) and the GCTF (3) programs, respectively. All image processing steps were carried out with RELION 3.0 (4).

For KCNQ1-CaM_{apo}, 2,957 micrographs were collected and 1,683,616 particles were auto-picked and extracted with a binning factor of 3 for 2D classification. The following two rounds of 3D classification with 1,370,276 selected particles were performed using the map of human KCNQ1-CaM complex (PDB: 6UZZ) (5) as a reference. After 3D classification, selected particles were combined and re-extracted to the pixel size of 1.014 Å for 3D refinement with a *C4* symmetry and Bayesian polishing via RELION 3.0. The final resolution of the EM map by 3D reconstruction of 169,344 particles was 3.5 Å.

For KCNQ1-CaM_{ML277}, 2,058 micrographs were collected and 1,197,453 particles were auto-picked and extracted with a binning factor of 3 for 2D classification. The following three rounds of 3D classification with 941,138 selected particles were performed using the map of KCNQ1-CaM_{apo} as a reference. After 3D classification, selected particles were combined and re-extracted to the pixel size of 1.014 Å for 3D refinement with a *C4* symmetry and Bayesian polishing via RELION 3.0. The final resolution of the EM map by 3D reconstruction of 200,556 particles was 2.6 Å.

For KCNQ1-CaM$_{\text{ML277-PIP2-A}}$ and KCNQ1-CaM$_{\text{ML277-PIP2-B}}$, 1,803 micrographs were collected and 1,018,488 particles were auto-picked and extracted with a binning factor of 3 for 2D classification. The following two rounds of 3D classification with 750,461 selected particles were performed using the map of KCNQ1-CaM$_{\text{ML277}}$ as a reference. After 3D classification, two different conformational 3D reconstructions were obtained, named KCNQ1-CaM$_{\text{ML277-PIP2-A}}$ and KCNQ1-CaM$_{\text{ML277-PIP2-B}}$, respectively. Then the selected particles were combined and re-extracted to the pixel size of 1.014 Å for 3D refinement with a *C4* symmetry and Bayesian polishing via RELION 3.0. The final resolution of the EM map by 3D reconstruction of KCNQ1-CaM$_{\text{ML277-PIP2-A}}$ (103,745 particles) was 3.1 Å, and the resulting 3D reconstruction of KCNQ1-CaM$_{\text{ML277-PIP2-B}}$ (257,550 particles) was 2.5 Å,

The resolution was estimated by applying a soft mask around the protein density and the gold-standard Fourier shell correlation (FSC) = 0.143 criterion. Local resolution maps were calculated with RELION 3.0.

Model building, refinement, and validation

De novo atomic models were built in Coot (6) based on the 2.6 Å resolution map of KCNQ1-CaM$_{\text{ML277}}$. The amino acid assignment was achieved based on the clearly defined density for bulky residues (Phe, Trp, Tyr, and Arg) and the model of KCNQ1-CaM complex (PDB: 6UZZ) (5) was used as a reference. PHENIX (7) was utilized for model refinement against cryo-EM maps using real-space refinement, with secondary structure restraints and non-crystallography symmetry applied. The models of KCNQ1-CaM$_{\text{apo}}$, KCNQ1-CaM$_{\text{ML277-PIP2-A}}$, and KCNQ1-CaM$_{\text{ML277-PIP2-B}}$ were built using the model of KCNQ1-CaM$_{\text{ML277}}$ as a template. The MolProbity (8) was used for model geometry statistics generation. The Van der Waals radii of the pore were calculated using HOLE (9). All figures were prepared in PyMoL (The PyMOL Molecular Graphics System, Version 1.8 Schrödinger, LLC.) and Chimera (10).

Electrophysiology

Constructs and mutagenesis: Overlap extension and high-fidelity PCR were used for generating KCNQ1 point mutations. Each mutation was verified by DNA sequencing. The mMessage T7 polymerase kit (Thermo Fisher Scientific) was then used for synthesizing cRNA of WT KCNQ1 and its mutations.

Oocyte expression: Stage V (or VI) oocytes were obtained from *Xenopus laevis* by laparotomy surgery, following the protocol approved by the Animal Studies Committee of Macau University of Science and Technology (Protocol #: MUST-NSFC-2021022601HPP). Oocytes were digested by collagenase (0.5 mg/ml, Sigma Aldrich, St Louis, MO) to remove the follicle membrane. KCNQ1 cRNAs (9.2 ng) were injected into each oocyte with a microinjector (RWD R-480 model). After injection, oocytes were kept in the ND96 solution (in mM): 96 NaCl, 2 KCl, 1.8 $CaCl_2$, 1 $MgCl_2$, 5 HEPES, 2.5 CH_3COCO_2Na, 1:100 Pen-Strep, pH 7.6) at 18°C for 2-6 days to allow sufficient KCNQ1 channel expression. All chemicals were purchased from Sigma Aldrich.

Two-electrode voltage clamp (TEVC): After channel expression, oocytes were transferred to a TEVC platform (Warner OC-725D amplifier + HEKA Patchmaster acquisition software) for whole-oocyte current recordings. Currents were sampled at 1 kHz and filtered at 2 kHz. Microelectrodes were made with a Sutter puller (P-1000) with resistances at ~1 MΩ when filled with 3 M KCl. For ML277 experiments, ML277 stock (Sigma Aldrich, in DMSO) was added to the bath and diluted to 1 μM. All recordings were performed at room temperature (21–23 °C).

Electrophysiology Data analysis: Data were analyzed with Clampfit (Axon Instruments, Inc., Sunnyvale, CA), Sigmaplot (SPSS, Inc., San Jose, CA), and IGOR (Wavemetrics, Lake Oswego, OR). G–V curves were fitted a Boltzmann equation $1/(1+\exp(-z*F*(V-V_{50})/RT))$, where V is the voltage, z is the equivalent valence, V_{50} is the half-maximal voltage, F is the Faraday constant, R is the gas constant, and T is the absolute temperature. For activation (τ_f and τ_s) and deactivation (τ_d) time constants of KCNQ1 currents in Figure 1, KCNQ1 activation currents were fitted with a double exponential equation to get the τ_f and τ_s for control, and were fitted separately with a single exponential function to get the τ_f and τ_s for currents after adding ML277.

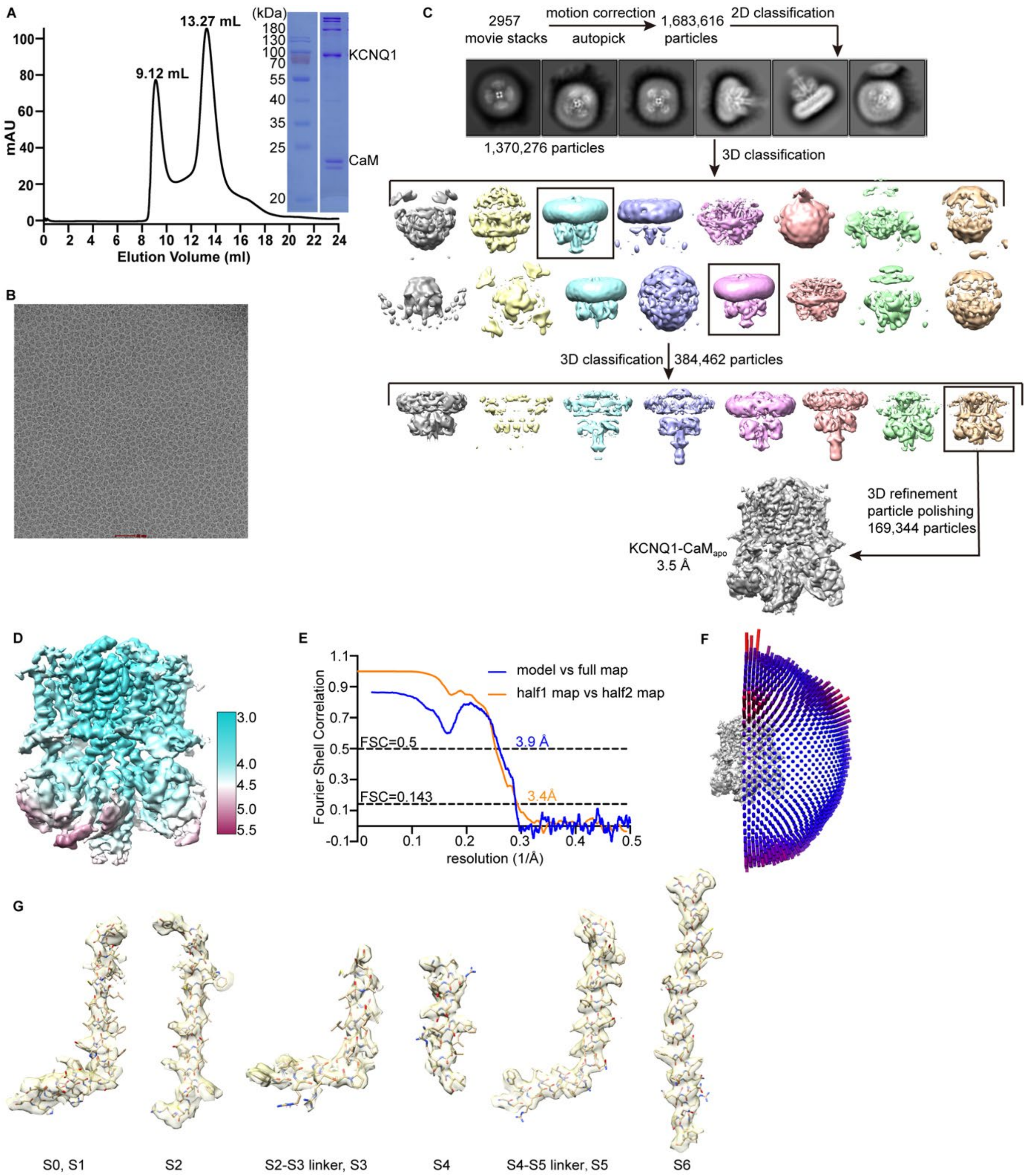

Fig. S1. Structure determination of KCNQ1-CaM$_{apo}$.

(A) Size-exclusion chromatography of KCNQ1-CaM$_{apo}$ on Superose 6 (GE Healthcare) and SDS-PAGE analysis of the final sample.

(B) Representative cryo-EM micrograph of KCNQ1-CaM$_{apo}$.

(C) Flowchart of image processing for KCNQ1-CaM$_{apo}$ particles.

(D) The density map of KCNQ1-CaM$_{apo}$ colored by local resolution. The local resolution was estimated with RELION 3.0 and generated in Chimera.

(E) The Gold-standard Fourier shell correlation (FSC) curves of the final 3D reconstruction of KCNQ1-CaM$_{apo}$, and the FSC curve for cross-validation between the map and the model of KCNQ1-CaM$_{apo}$.

(F) Euler angle distribution of KCNQ1-CaM$_{apo}$ particles used in the final 3D reconstruction, with the heights of the cylinders corresponding to the number of particles.

(G) Sample maps of the KCNQ1-CaM$_{apo}$ structure. The S4 and C-terminal half of S3 seem dynamic and are resolved in a relatively lower resolution.

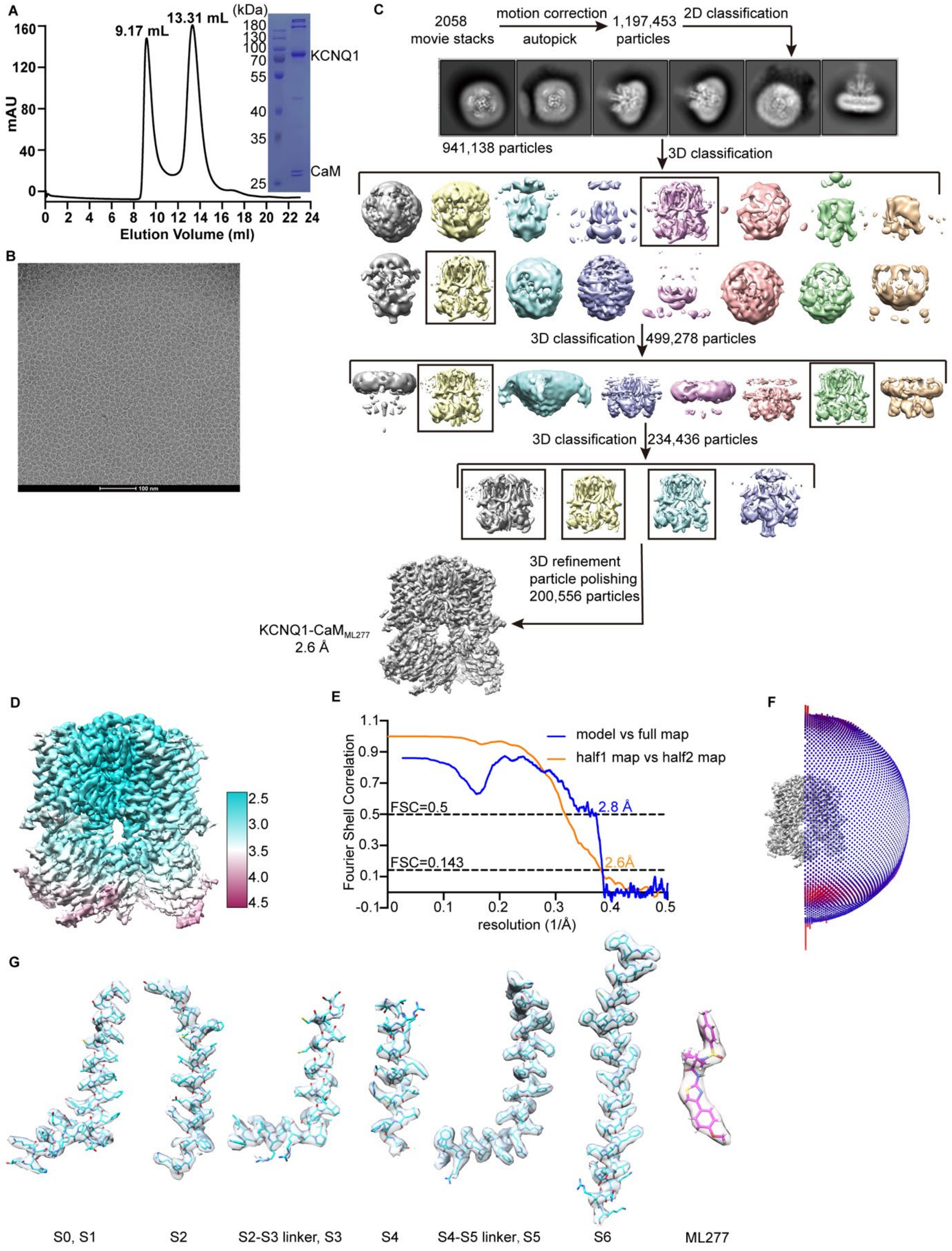

Fig. S2. Structure determination of KCNQ1-CaM$_{ML277}$.

(A) Size-exclusion chromatography of KCNQ1-CaM$_{ML277}$ on Superose 6 (GE Healthcare) and SDS-PAGE analysis of the final sample.

(B) Representative cryo-EM micrograph of KCNQ1-CaM$_{ML277}$.

(C) Flowchart of image processing for KCNQ1-CaM$_{ML277}$ particles.

(D) The density map of KCNQ1-CaM$_{ML277}$ colored by local resolution. The local resolution was estimated with RELION 3.0 and generated in Chimera.

(E) The Gold-standard Fourier shell correlation (FSC) curves of the final 3D reconstruction of KCNQ1-CaM$_{ML277}$, and the FSC curve for cross-validation between the map and the model of KCNQ1-CaM$_{ML277}$.

(F) Euler angle distribution of KCNQ1-CaM$_{ML277}$ particles used in the final 3D reconstruction, with the heights of the cylinders corresponding to the number of particles.

(G) Sample maps of the KCNQ1-CaM$_{ML277}$ structure.

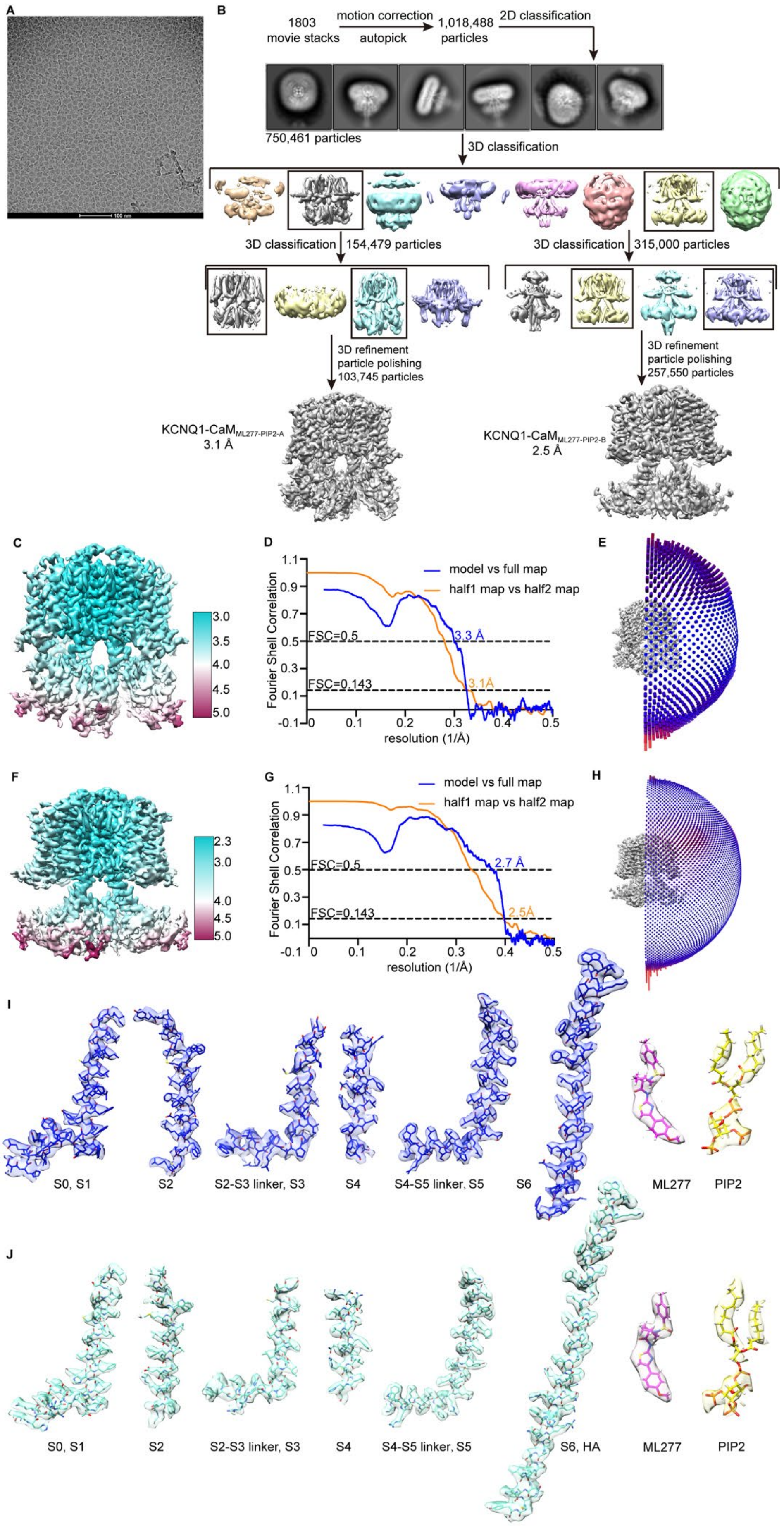
A
100 nm
B
1803
movie stacks
motion correction
autopick
1,018,488
particles
2D classification
750,461 particles
3D classification
3D classification
154,479 particles
3D classification
315,000 particles
3D refinement
particle polishing
103,745 particles
3D refinement
particle polishing
257,550 particles
KCNQ1-CaM$_{ML277-PIP2-A}$
3.1 Å
KCNQ1-CaM$_{ML277-PIP2-B}$
2.5 Å
C
3.0
3.5
4.0
4.5
5.0
D
Fourier Shell Correlation
model vs full map
half1 map vs half2 map
FSC=0.5
FSC=0.143
3.3 Å
3.1Å
resolution (1/Å)
1.1
0.9
0.7
0.5
0.3
0.1
-0.1
0
0.1
0.2
0.3
0.4
0.5
E
F
2.3
3.0
4.0
4.5
5.0
G
Fourier Shell Correlation
model vs full map
half1 map vs half2 map
FSC=0.5
FSC=0.143
2.7 Å
2.5Å
resolution (1/Å)
1.1
0.9
0.7
0.5
0.3
0.1
-0.1
0
0.1
0.2
0.3
0.4
0.5
H
I
S0, S1
S2
S2-S3 linker, S3
S4
S4-S5 linker, S5
S6
ML277
PIP2
J
S0, S1
S2
S2-S3 linker, S3
S4
S4-S5 linker, S5
S6, HA
ML277
PIP2

Fig. S3. Structure determination of KCNQ1-CaM$_{\text{ML277-PIP2}}$.

(A) Representative cryo-EM micrograph of KCNQ1-CaM$_{\text{ML277-PIP2}}$.

(B) Flowchart of image processing for KCNQ1-CaM$_{\text{ML277-PIP2}}$ particles.

(C) The density map of KCNQ1-CaM$_{\text{ML277-PIP2-A}}$ colored by local resolution. The local resolution was estimated with RELION 3.0 and generated in Chimera.

(D) The Gold-standard Fourier shell correlation (FSC) curves of the final 3D reconstruction of KCNQ1-CaM$_{\text{ML277-PIP2-A}}$, and the FSC curve for cross-validation between the map and the model of KCNQ1-CaM$_{\text{ML277-PIP2-A}}$.

(E) Euler angle distribution of KCNQ1-CaM$_{\text{ML277-PIP2-A}}$ particles used in the final 3D reconstruction, with the heights of the cylinders corresponding to the number of particles.

(F) The density map of KCNQ1-CaM$_{\text{ML277-PIP2-B}}$ colored by local resolution. The local resolution was estimated with RELION 3.0 and generated in Chimera.

(G) The Gold-standard Fourier shell correlation (FSC) curves of the final 3D reconstruction of KCNQ1-CaM$_{\text{ML277-PIP2-B}}$, and the FSC curve for cross-validation between the map and the model of KCNQ1-CaM$_{\text{ML277-PIP2-B}}$.

(H) Euler angle distribution of KCNQ1-CaM$_{\text{ML277-PIP2-B}}$ particles used in the final 3D reconstruction, with the heights of the cylinders corresponding to the number of particles.

(I) Sample maps of the KCNQ1-CaM$_{\text{ML277-PIP2-A}}$ structure.

(J) Sample maps of the KCNQ1-CaM$_{\text{ML277-PIP2-B}}$ structure.

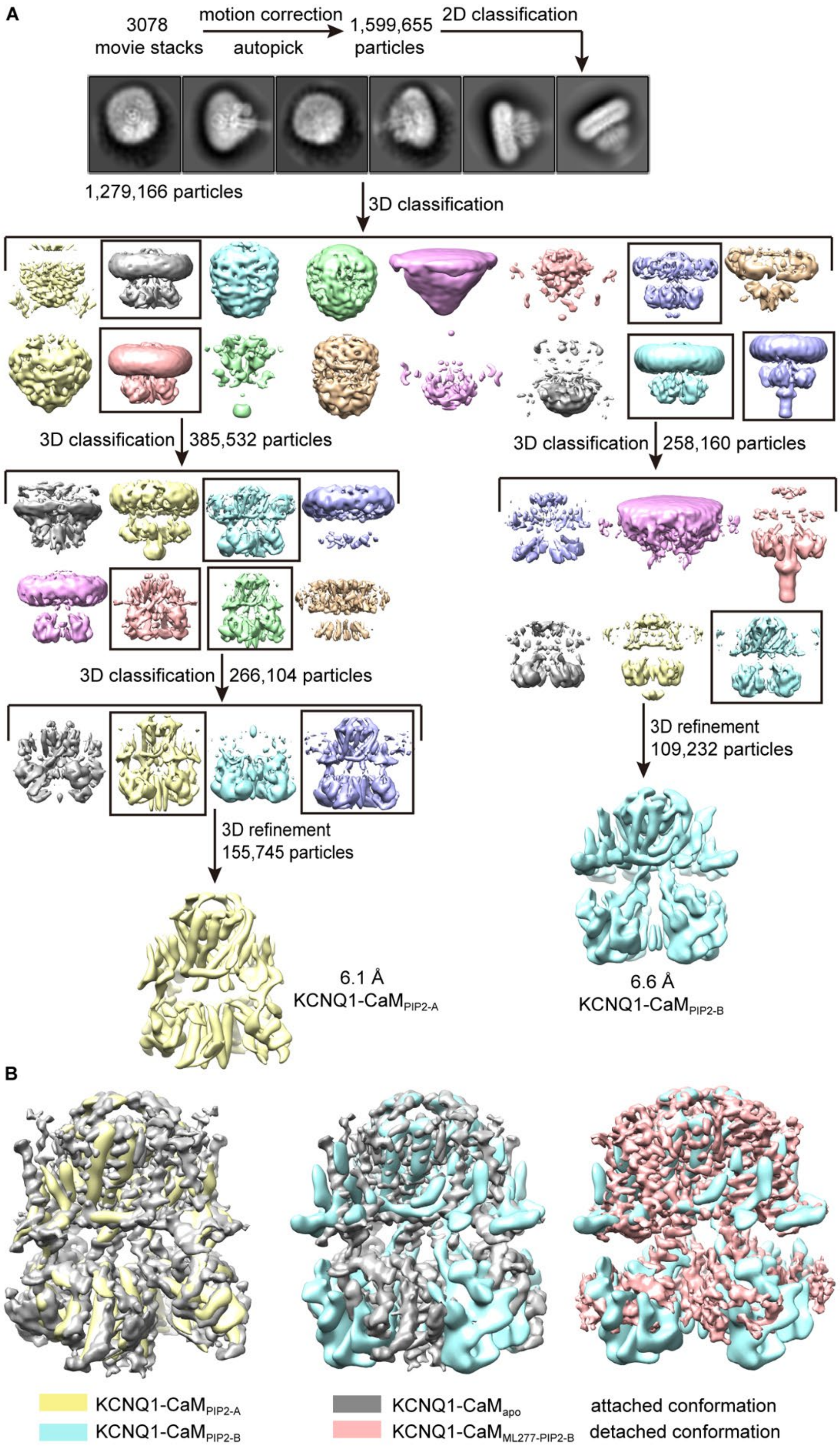

Fig. S4. Structure determination of KCNQ1-CaM$_{\text{PIP2}}$.

(A) Flowchart of image processing for KCNQ1-CaM$_{\text{PIP2}}$ particles.

(B) Map comparisons of KCNQ1-CaM$_{\text{apo}}$ (gray) and KCNQ1-CaM$_{\text{PIP2-A}}$ (yellow), KCNQ1-

$\mathrm{CaM_{apo}}$ (gray) and KCNQ1-$\mathrm{CaM_{PIP2\text{-}B}}$ (cyan), and KCNQ1-$\mathrm{CaM_{PIP2\text{-}B}}$ (cyan) and KCNQ1-$\mathrm{CaM_{ML277\text{-}PIP2\text{-}B}}$ (salmon). While KCNQ1-$\mathrm{CaM_{PIP2\text{-}A}}$ adopts an attached conformation like KCNQ1-$\mathrm{CaM_{apo}}$, KCNQ1-$\mathrm{CaM_{PIP2\text{-}B}}$ is in an intermediate conformation between the attached (KCNQ1-$\mathrm{CaM_{apo}}$) and detached conformation (KCNQ1-$\mathrm{CaM_{ML277\text{-}PIP2\text{-}B}}$).

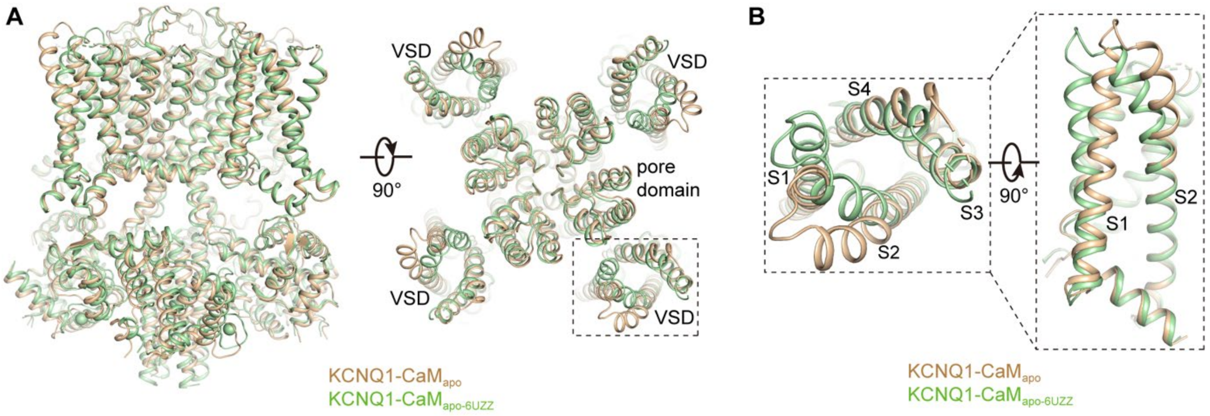

Fig. S5. Structural comparison of KCNQ1-CaM$_{apo}$ and KCNQ1-CaM$_{apo-6UZZ}$.

(A) Structural comparison between KCNQ1-CaM$_{apo}$ (wheat) and KCNQ1-CaM$_{apo-6UZZ}$ (green) in the side view (left) and top view (right).

(B) Superposition of VSDs in KCNQ1-CaM$_{apo}$ (wheat) and KCNQ1-CaM$_{apo-6UZZ}$ (green) in top view (left) and side view (right).

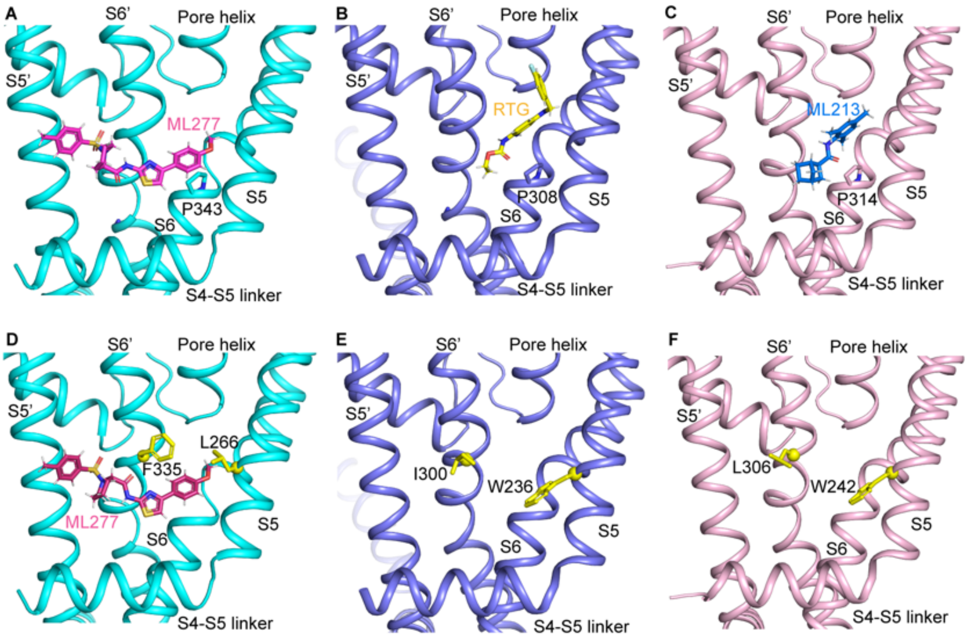

G

Sequence alignment of S5

```
              266
KCNQ1  HRQELITTLYIGFLGLIFSSYFVYLAEK
KCNQ2  HSKELVTAWYIGFLCLILASFLVYLAEK
KCNQ3  HSKELITAWYIGFLTLILSSFLVYLVEK
KCNQ4  HSKELITAWYIGFLVLIFASFLVYLAEK
KCNQ5  HSKELITAWYIGFLVLIFSSFLVYLVEK
```

Sequence alignment of S6

```
                  335
KCNQ1  WVGKTIASCFSVFAISFFALPAGILGSGFALKVQQ
KCNQ2  WNGRLLAATFTLIGVSFFALPAGILGSGFALKVQE
KCNQ3  WEGRLIAATFSLIGVSFFALPAGILGSGLALKVQE
KCNQ4  WLGRVLAAGFALLGISFFALPAGILGSGFALKVQE
KCNQ5  WLGRLLSAGFALLGISFFALPAGILGSGFALKVQE
```

Fig. S6. Comparison of binding sites of ML277, retigabine (RTG), and ML213 in KCNQ channels.

(A) The ML277 binding site in KCNQ1-CaM$_{\mathrm{ML277}}$. The side chain of Pro343 in S6 is shown as sticks.

(B) The RTG binding site in KCNQ2-CaM$_{\mathrm{RTG}}$ (PDB: 7CR2). The side chain of Pro308 in S6 is shown as sticks.

(C) The ML213 binding site in KCNQ4-CaM$_{\mathrm{ML213}}$ (PDB: 7VNQ). The side chain of Pro314 in S6 is shown as sticks.

(D) The Phe335 and Leu266 in KCNQ1-CaM$_{\mathrm{ML277}}$.

(E) The Ile300 and Trp236 in KCNQ2-CaM$_{\mathrm{RTG}}$ (PDB: 7CR2).

(F) The Leu306 and Trp242 in KCNQ4-CaM$_{\mathrm{ML213}}$ (PDB: 7VNQ).

(G) Sequence alignment of S5 and S6 segments among human KCNQ family members.

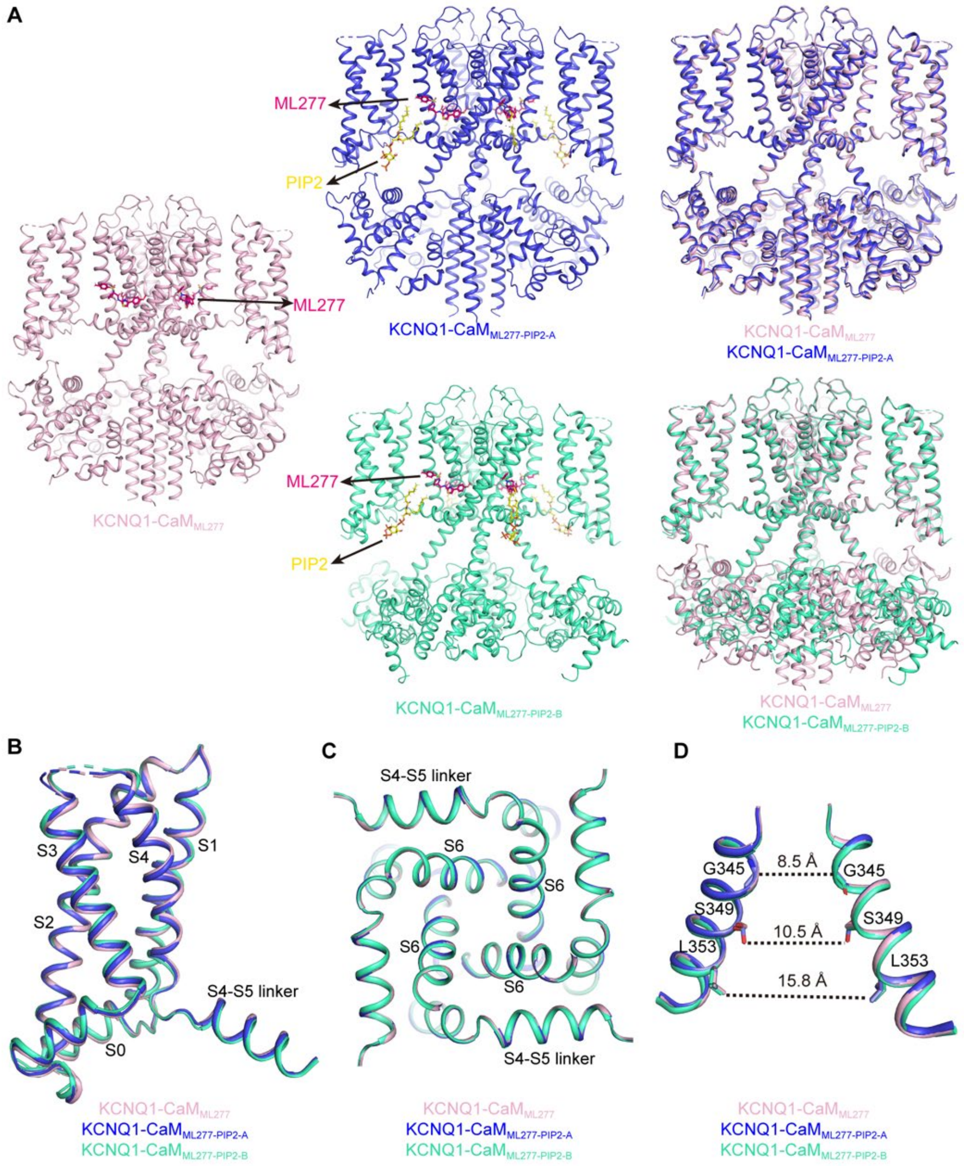

Fig. S7. Structural comparison of KCNQ1-CaM$_{\text{ML277}}$, KCNQ1-CaM$_{\text{ML277-PIP2-A}}$ and KCNQ1-CaM$_{\text{ML277-PIP2-B}}$.

(A) Comparisons of overall structures of KCNQ1-CaM$_{\text{ML277}}$ (pink) and KCNQ1-CaM$_{\text{ML277-PIP2-A}}$ (blue), and KCNQ1-CaM$_{\text{ML277}}$ and KCNQ1-CaM$_{\text{ML277-PIP2-B}}$ (green).

(B) Structural comparison of VSDs in KCNQ1-CaM$_{\text{ML277}}$, KCNQ1-CaM$_{\text{ML277-PIP2-A}}$ and KCNQ1-CaM$_{\text{ML277-PIP2-B}}$.

(C) Structural comparison of PDs in KCNQ1-CaM$_{\text{ML277}}$, KCNQ1-CaM$_{\text{ML277-PIP2-A}}$, and KCNQ1-CaM$_{\text{ML277-PIP2-B}}$ in the bottom view.

(D) Structural comparison of the activation gates in KCNQ1-CaM$_{\text{ML277}}$, KCNQ1-CaM$_{\text{ML277-PIP2-A}}$, and KCNQ1-CaM$_{\text{ML277-PIP2-B}}$ in the side view.

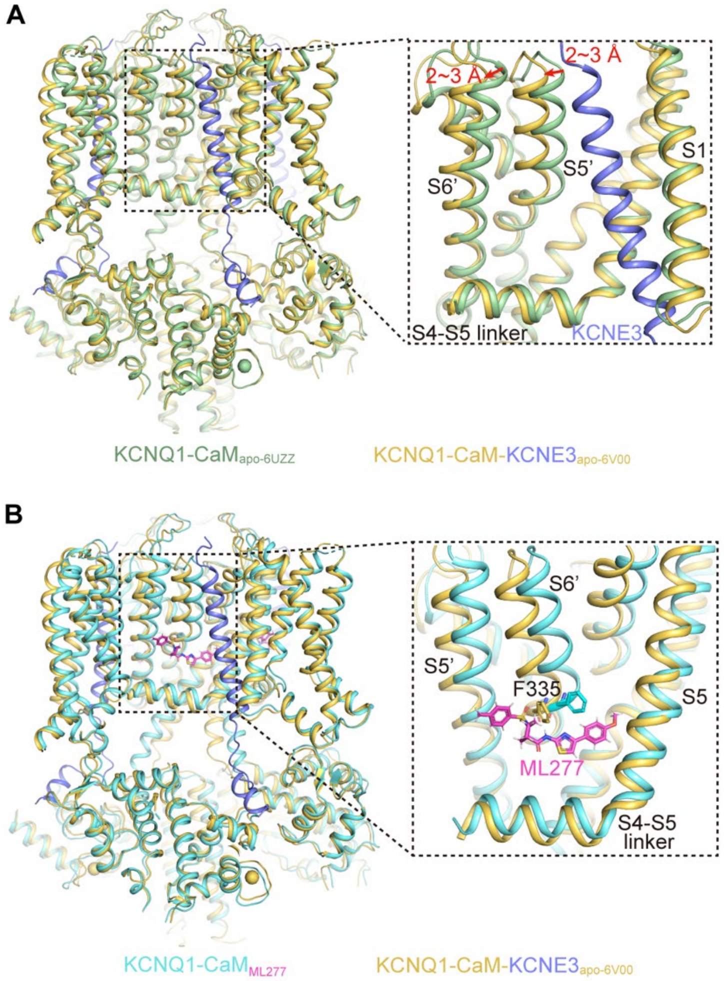

Fig S8. Structural comparison indicates that KCNE3 may alter interactions between ML277 and KCNQ1.

(A) Structural comparison of KCNQ1-CaM$_{\text{apo-6UZZ}}$ and KCNQ1-CaM-KCNE3$_{\text{apo-6V00}}$. Red arrows indicate the shift of S5 and S6 upon KCNE3 binding.

(B) Structural comparisons of KCNQ1-CaM$_{\text{ML277}}$ and KCNQ1-CaM-KCNE3$_{\text{apo-6V00}}$. ML277 would form clashes with the Phe335 side chain if it bound to the KCNQ1-CaM-KCNE3 complex.

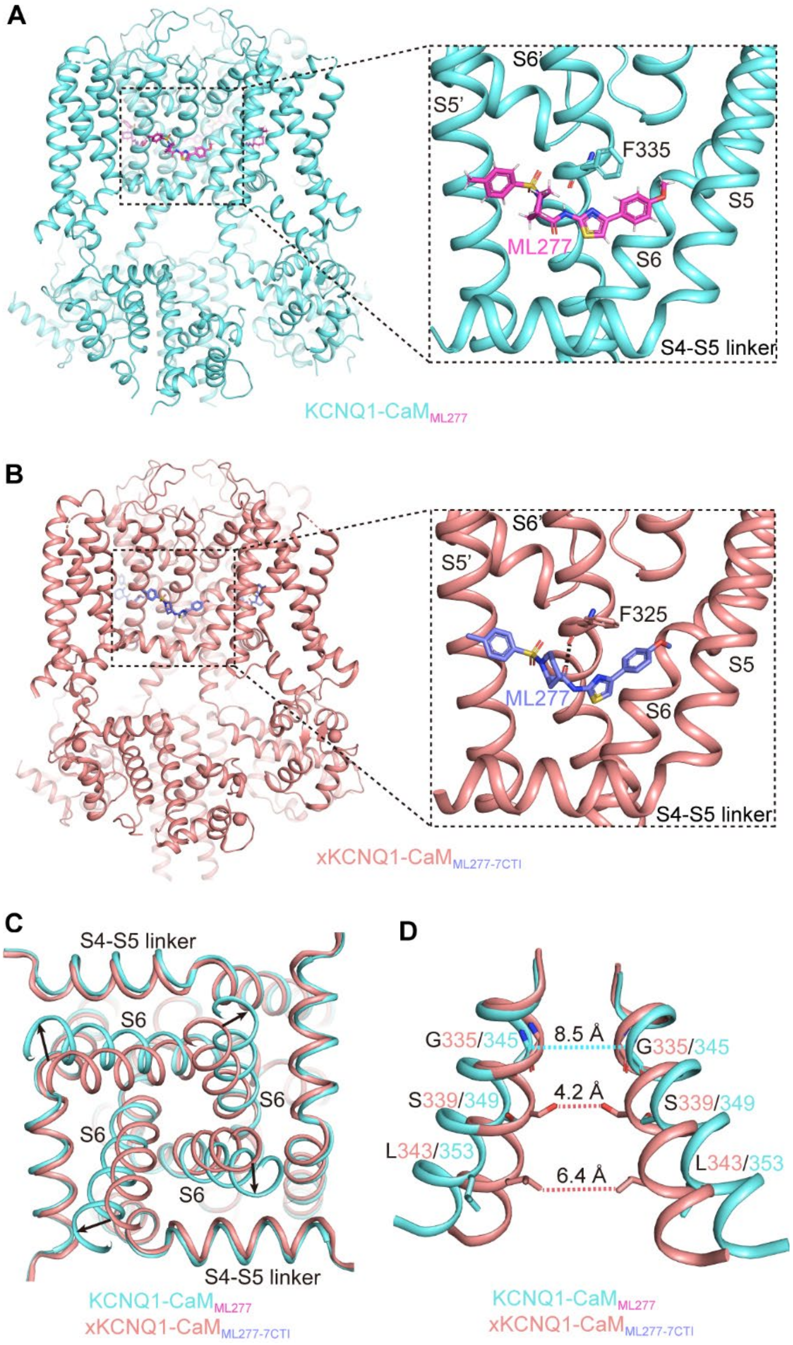

Fig S9. Structural comparison of KCNQ1-CaM$_{\mathrm{ML277}}$ and xKCNQ1-CaM$_{\mathrm{ML277\text{-}7CTI}}$.

(A) ML277 bound in KCNQ1-CaM$_{\mathrm{ML277}}$. Side chain of Phe335 is shown as sticks.

(B) ML277 bound in xKCNQ1-CaM$_{\mathrm{ML277\text{-}7CTI}}$. The dashed line indicates the electrostatic repulsion between the carbonyl in ML277 and the mainchain carbonyl of Phe335.

(C) Structural differences of PDs in KCNQ1-CaM$_{\mathrm{ML277}}$ and xKCNQ1-CaM$_{\mathrm{ML277\text{-}7TCI}}$ in the bottom view.

(D) Structural differences of the activation gates in KCNQ1-CaM_{ML277} and xKCNQ1-$CaM_{ML277\text{-}7CTI}$ in the side view. The dashed lines show diagonal atom-to-atom distances between constriction-forming residues (in Å). The gate in KCNQ1-CaM_{ML277} opens up but in xKCNQ1-$CaM_{ML277\text{-}7CTI}$ remains closed.

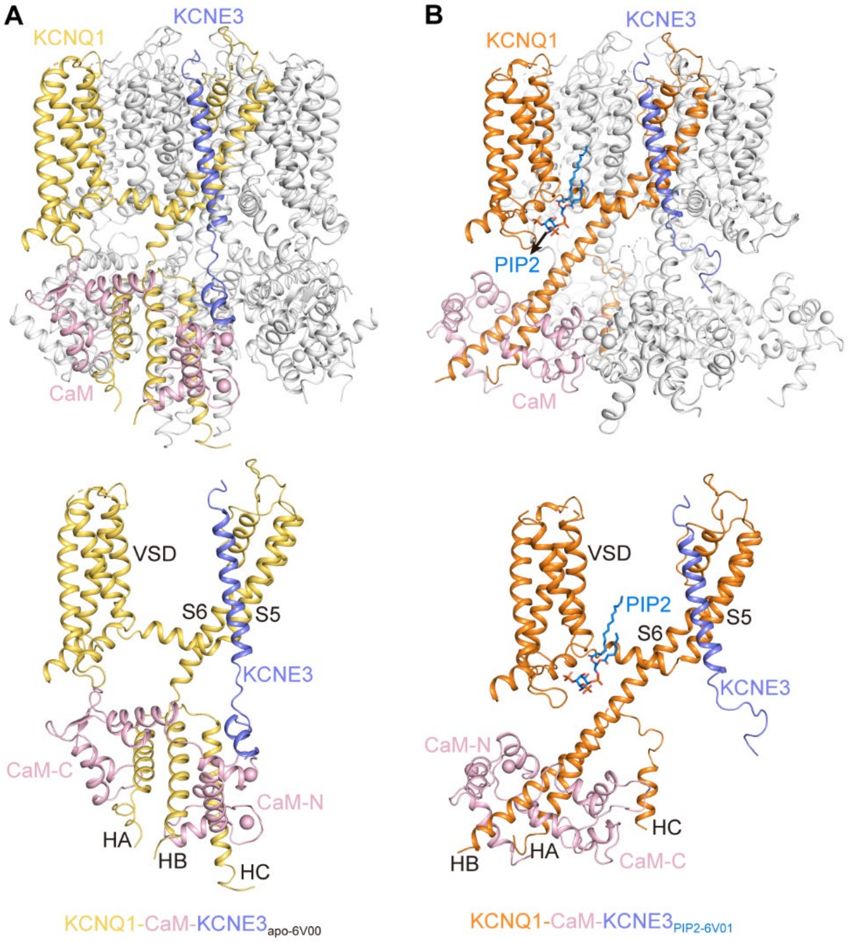

Fig S10. Structural comparisons of KCNQ1-CaM-KCNE3$_{apo\text{-}6V00}$ and KCNQ1-CaM-KCNE3$_{PIP2\text{-}6V01}$.

(A) The overall structure of KCNQ1-CaM-KCNE3$_{apo\text{-}6V00}$ and one copy of KCNQ1, CaM, and KCNE3. S6 and HA are connected by a loop linker and the gate is closed.

(B) The overall structure of KCNQ1-CaM-KCNE3$_{PIP2\text{-}6V01}$ and one copy of KCNQ1, CaM, KCNE3, and PIP_2. PIP_2 binds at the cleft formed by the S2-S3 linker, S3, S4, and S4-S5 linker. Upon the PIP_2 binding, CTD and CaM undergo an almost 180° rotation, along with the formation of a continuous helix by S6 and HA and the opening of the activation gate.

Supplementary Table S1. Data collection and refinement statistics.

	KCNQ1-CaM$_{\text{apo}}$	KCNQ1-CaM$_{\text{ML277}}$	KCNQ1-CaM$_{\text{ML277-PIP2-A}}$	KCNQ1-CaM$_{\text{ML277-PIP2-B}}$
Data collection and processing				
Magnification	49310	49310	49310	49310
Voltage (kV)	300	300	300	300
Electron exposure (e-/Å^2)	~ 64	~ 64	~ 64	~ 64
Defocus range (μm)	-1.1 to -1.3	-1.1 to -1.3	-1.1 to -1.3	-1.1 to -1.3
Pixel size (Å)	1.014	1.014	1.014	1.014
Symmetry imposed	*C4*	*C4*	*C4*	*C4*
Initial particle images (no.)	1,683,616	1,197,453	1,018,488	1,018,488
Final particle images (no.)	169,344	200,556	103,745	257,550
Map resolution (Å)	3.5	2.6	3.1	2.5
FSC threshold	0.143	0.143	0.143	0.143
Refinement				
Initial model used (PDB code)	KCNQ1-CaM$_{\text{ML277}}$	6UZZ		
Model resolution (Å)	3.4		3.3	2.7
FSC threshold	0.143	0.143	0.143	0.143
Map sharpening B factor (Å^2)	-70	-40	-60	-30
Model composition				
Non-hydrogen atoms	15716	15848	16040	14284
Protein residues	1968	1968	1968	1896
ligands	0	4	8	8
B factors (Å^2)				
Protein	176.52	104.94	109.05	118.18
R.m.s. deviations				
Bond lengths (Å)	0.012	0.020	0.013	0.025
Bond angles (°)	1.371	1.226	1.083	1.203
Validation				
MolProbity score	2.14	1.13	1.40	2.28
Clashscore	20.98	1.81	3.42	17.54
Rotamer outliers (%)	0.00	0.73	0.00	0.00
Ramachandran plot				
Favored (%)	95.30	96.90	96.13	90.45
Allowed (%)	4.49	3.10	3.87	9.55
Outliers (%)	0.21	0.00	0.00	0.00

Supplementary Movies:

Movie S1. ML277-induced conformational changes of KCNQ1-CaM in the context of the whole channel complex.

Movie S2. ML277-induced conformational changes of one KCNQ1 subunit.

Movie S3. ML277-induced opening of the activation gate of KCNQ1 in the bottom view.

Movie S4. PIP_2-induced structural rearrangement of CTD and CaM in the context of the whole channel complex.

Movie S5. PIP_2-induced structural rearrangement of CTD and CaM in one KCNQ1 subunit.

Movie S6. PIP_2-induced structural rearrangement of CTD (HA, HB, and HC) in the top view with the TMD omitted for clarity.

Supplementary References

1. D. N. Mastronarde, Automated electron microscope tomography using robust prediction of specimen movements. *J Struct Biol* **152**, 36-51 (2005).
2. S. Q. Zheng *et al.*, MotionCor2: anisotropic correction of beam-induced motion for improved cryo-electron microscopy. *Nat Methods* **14**, 331-332 (2017).
3. K. Zhang, Gctf: Real-time CTF determination and correction. *J Struct Biol* **193**, 1-12 (2016).
4. S. H. W. Scheres, RELION: Implementation of a Bayesian approach to cryo-EM structure determination. *J Struct Biol* **180**, 519-530 (2012).
5. J. Sun, R. MacKinnon, Structural basis of human KCNQ1 modulation andgating. *Cell* **180**, 340-347 e349 (2020).
6. P. Emsley, B. Lohkamp, W. G. Scott, K. Cowtan, Features and development of Coot. *Acta Crystallogr D* **66**, 486-501 (2010).
7. P. D. Adams *et al.*, PHENIX: a comprehensive Python-based system for macromolecular structure solution. *Acta Crystallographica Section D-Structural Biology* **66**, 213-221 (2010).
8. V. B. Chen *et al.*, MolProbity: all-atom structure validation for macromolecular crystallography. *Acta Crystallographica Section D-Structural Biology* **66**, 12-21 (2010).
9. O. S. Smart, J. G. Neduvelil, X. Wang, B. A. Wallace, M. S. P. Sansom, HOLE: A program for the analysis of the pore dimensions of ion channel structural models. *J Mol Graph Model* **14**, 354-& (1996).
10. E. F. Pettersen *et al.*, UCSF Chimera--a visualization system for exploratory research and analysis. *J Comput Chem* **25**, 1605-1612 (2004).